Investigation of the oxidation mechanisms of superlattice Cr-CrN/TiSiN-Cr multilayer coatings on Zircaloy substrates under high-temperature steam atmospheres

Junkai Liu [a,b], Zhe Hao [a], Zhexin Cui [a], Dayan Ma [c], Junqiang Lu [d], Yanguang Cui [d], Chong Li [d], Wenbo Liu [a], Shijing Xie [a], Ping Huang [c], Guanghai Bai [e], Di Yun [a,f,*]

[a] School of Nuclear Science and Technology, Xi'an Jiaotong University, Xi'an 710049, China
[b] Institute for Applied Materials (IAM), Karlsruhe Institute of Technology (KIT), D-76021 Karlsruhe, Germany
[c] State-key Lab for Mechanical Behavior of Materials, Xi'an Jiaotong University, Xi'an 710049, China
[d] Shanghai Nuclear Engineering Research & Design Institute, Shanghai 200233, China
[e] Suzhou Nuclear Power Research Institute, Suzhou 215004, China
[f] Key Laboratory of Thermo-Fluid Science and Engineering of MOE, School of Energy and Power Engineering, Xi'an Jiaotong University, 28 Xianning West Road, Xi'an 710049, China

ARTICLE INFO

Keywords:
ATF cladding
High-temperature steam oxidation
Superlattice structure
Nitride coating
Microstructural evolution

ABSTRACT

Cr-CrN/TiSiN-Cr multilayer coatings were deposited on Zircaloy substrates by multi-arc ion plating, and the microstructure and oxidation behavior of the as-deposited coatings, specifically the middle CrN/TiSiN layer, were investigated. The CrN/TiSiN layer exhibited a superlattice structure. The multilayer coatings effectively protected the Zircaloy substrates from oxidation. $(Cr_{1-x}Ti_x)_2O_3$ and Cr_2TiO_5 phases were produced in the coating after oxidation at 1200 °C for 1500 s. With oxidation time increases, most of the Cr atoms in these two phases were replaced by Ti atoms. Oxidation mechanisms of the as-deposited coatings are discussed and a decomposition model of the superlattice CrN/TiSiN layer is proposed.

1. Introduction

Zirconium alloys (Zircaloy) have been used as nuclear reactor fuel cladding materials for more than 50 years owing to their various advantages such as low neutron absorption cross-section, outstanding high-temperature water corrosion resistance, high thermal conductivity, excellent mechanical properties, and promising irradiation resistance [1–4]. However, under loss-of-coolant accident conditions, Zircaloy severely reacts with high-temperature steam, which produces a large amount of H_2 and heat, further causing H_2 explosion and serious accidents in nuclear power plants [5–8]. After the Fukushima accident in 2011, research and development of innovative accident-tolerant fuels (ATFs), which are safer, more reliable, and economical, has been accelerated in the nuclear industry worldwide [9–11]. ATFs not only can significantly improve the accident tolerance of commercial nuclear reactors, particularly by reducing H_2 generation and heat release during oxidation, but can also replace the existing fuel system technology to further improve the safety and competitiveness of these reactors. Among the various ATFs, surface-coated Zircaloy substrates are the most developed candidate materials [12]. By depositing surface coatings with excellent high-temperature oxidation resistances on Zircaloy substrates, severe oxidation of these substrates can be effectively delayed, and more time margin can be provided to cope with accidents [13–19]. Furthermore, the existing advantages of the current commercial Zircaloy can be completely utilized without considerably changing the design of the present reactors and nuclear fuels. Therefore, surface-coated Zircaloy has been considered as one of the most promising candidate materials for application in the nuclear power plant industry. Among the current coatings, pure Cr coating with optimal oxidation and corrosion resistance and excellent mechanical properties is deemed the best surface coating for Zircaloy substrates [14,15,18–21]. However, there are still several limitations of Cr-coated Zircaloy substrate systems: 1) the inward diffusion of Cr from coating to substrate, which decreases the thickness of the coating [22]; 2) selective oxidation of the outward diffused Zr at the grain boundaries of the coating, and the resulting oxidation products afford O diffusion paths and cause the transition of

* Corresponding author at: School of Nuclear Science and Technology, Xi'an Jiaotong University, Xi'an 710049, China.
E-mail address: diyun1979@xjtu.edu.cn (D. Yun).

oxidation kinetics [15]; 3) Cr–Zr eutectic reaction at temperatures above 1332 °C, which forms a liquid phase and affects the structural integrity of the coating [15]; and 4) during oxidation, the thickness of the protective Cr_2O_3 scale can be decreased through the reduction reaction between Cr_2O_3 and Zr, and this thickness decrease destroys the protective function of the coating [14,19]. Thus, it is still necessary to investigate and establish other types of coatings that may avoid the shortcomings of Cr-coated Zircaloy substrate systems.

Nitride coatings, including CrN coatings, have been widely applied in the field of cutting tools and molds owing to their superior mechanical properties and excellent oxidation resistance [16,23]. To further improve the comprehensive properties of CrN coatings, multi-element hard coatings were designed by adding different elements, such as Al, Si, Ti, and Y, to CrN coatings and extensively analyzed [17,24,25]. Subsequently, the mechanical properties and oxidation resistance of nitride coatings were significantly improved. In our previous studies [16,17], CrN and multi-element hard coatings, including CrAlN and CrAlSiN coatings, on the surfaces of Zircaloy substrates exhibited excellent oxidation resistances when exposed to a high-temperature steam atmosphere up to 1200 °C. Moreover, nitride coatings can efficiently inhibit the outward diffusion and the selective oxidation of Zr inside the coating, which are considered the most serious problems in Cr-coated Zr substrate systems and are the primary reasons for the failure of coatings during oxidation. Nevertheless, nitride coatings are unstable at temperatures above 940 °C because decomposition and N_2 release occur at these temperatures [16,17,26]. N_2 release at high temperatures can lead to the formation of N_2 bubbles inside the coating and pores inside the oxide scale and at the coating/substrate interface. These bubbles and pores affect the structural integrity of the nitride coating. Multi-element hard coatings with superlattice structures composed of nanoscale multilayer sequences of two or more materials showed superior mechanical properties, higher thermal stabilities, and better oxidation resistance [27–31]. Therefore, the introduction of a superlattice structure may be deemed as an effective approach to solve the current problems of conventional monolithic nitride coatings. In addition, the multilayer structure may serve as a defect sink to diverge irradiation-induced defects such that they do not form clusters, which are detrimental to the integrity of the coating [32].

Surface coatings with superlattice structures have been systematically investigated and utilized in other fields owing to their excellent comprehensive properties. However, only few studies have been conducted on the evaluation of superlattice-coated Zircaloy as an accident-tolerant fuel cladding candidate material. Furthermore, the oxidation behavior and oxidation mechanisms of superlattice coatings in steam at temperatures up to 1200 °C have rarely been examined. Consequently, in this study, triple-layer coatings with middle CrN/TiSiN superlattice layers were deposited on the surfaces of Zircaloy substrates. Structures of the as-deposited coatings were analyzed in detail. Oxidation behaviors of the coatings in steam were studied at high temperatures up to 1200 °C, and the oxidation mechanisms of the coatings were discussed.

2. Experimental

Herein, the following Zircaloy substrates were used: commercial Zircaloy-4 (Zry-4, Zr—1.5Sn—0.2Fe—0.1Cr) solid rods with diameters of ~10 mm and lengths of ~10 mm and Zry-A (Zr—1Sn—1Nb—0.1Fe) tubes with outer diameters of ~9.5 mm, lengths of ~10 mm, and wall thicknesses of ~0.7 mm. A threaded hole of size M3 was drilled at the bottom of the samples to hang the samples in a vacuum chamber during coating deposition. Before coating deposition, all Zircaloy samples were pickled in a mixed acid solution (10 vol% hydrofluoric acid + 45 vol% nitric acid + 45 vol% water) to remove the oxide layer on the surface of the samples and reduce the surface roughness. After pickling, ultrasonic cleaning was successively performed in acetone and ethanol for 900 s followed by drying in hot air to clean the surface of the samples. Multi-arc ion plating was employed for coating deposition, and specific deposition was conducted as follows:

1) Ion etching under an Ar atmosphere for 1200 s at a flow rate of 3 mL/s and a vacuum degree of 0.7 Pa to clean the surface of the samples.
2) Deposition of a Cr interlayer for 1200 s at an Ar flow rate of 2 mL/s and a vacuum degree of 0.5 Pa; a high-purity Cr target (99.9%) was used, and arc current was controlled at 100 A. The purpose of depositing a Cr interlayer is to strengthen the adhesion between the nitride coating and the Zircaloy substrate.
3) Deposition of a CrN/TiSiN superlattice coating for ~10,800 s under a N_2 atmosphere at a flow rate of 8.3 mL/s and a vacuum degree of 1.2 Pa. The same abovementioned Cr target and a $Ti_{85}Si_{15}$ (99.9%) target were utilized and symmetrically installed on opposite sides. All arc currents were 100 A.
4) Deposition of a Cr outer layer under the same conditions as abovementioned in 2). This Cr outer layer is to improve the mechanical compatibility of the inner nitride coating, and prevent the nitride coating from cracking due to the mismatch of the thermal expansion coefficient between the nitride coating and the Zircaloy substrate when the sample is under extreme conditions of rapid heating up or cooling down.

During the entire deposition process, the samples were installed on a rotation bracket and rotated at a speed of 15 Hz. During coating deposition, temperature was maintained below 400 °C to prevent phase transformation of Zircaloy substrates.

A synchrotron thermogravimetric analysis system (STA, NETZSCH STA 449F) was used to analyze isothermal oxidation behavior of bare and as-deposited samples under a steam atmosphere at 1000 and 1200 °C. The STA can provide information about the mass change of the samples in situ during steam oxidation. In the first step, the furnace of the STA was vacuumed. Then, the furnace was heated from 30 °C at a heating rate of 5 K/60 s to the designated temperature of 1000 or 1200 °C. High-purity Ar at a flow rate of 2.5 mL/s was injected into the furnace to protect the samples from oxidation during heating. When the temperature in the furnace reached the predefined value, steam preheated at 150 °C at a flow rate of 1.5 g/3600 s was introduced into the furnace. The isothermal oxidation time at 1000 °C was 3600 s, whereas the isothermal oxidation times at 1200 °C were 1500 s and 3600 s. When isothermal oxidation was completed, the steam injection was stopped, Ar was continuously introduced into the furnace to protect the samples, and the samples were cooled inside the furnace.

X-ray diffraction (XRD) was performed using an X-ray diffractometer (Bruker D8 Focus) to study the surface phases of the coated samples before and after high-temperature steam oxidation. The diffraction source was Cu Kα (λ 1.5406 Å), the 2θ range was 20–100°, and the scanning step was 0.02°. X-ray photoelectron spectroscopy (XPS, Thermo Fisher ESCALAB Xi^+) with an Al Kα (h_ν 1486.6 eV) radiation source was used to analyze the binding energy of each element inside the coating. Before XPS, the surfaces of the samples were polished to remove most part of the outer Cr layer. Scanning electron microscopy (SEM, GeminiSEM 500) coupled with energy-dispersive X-ray spectroscopy (EDS, Oxford) was used to characterize the surface and cross-sectional microstructures of the samples before and after steam oxidation. The samples used for cross-sectional microstructural characterization were initially embedded in epoxy resin and were then cut along the central axis by a low-speed cutting machine, followed by grinding and polishing to a mirror surface; finally, they were ultrasonically cleaned and dried. Transmission electron microscopy (TEM, JEOL JEM-F200) was utilized to further comprehensively characterize the microstructures of the as-deposited coatings. Specimen for TEM was prepared using a focused ion beam (FIB, Helios Nanolab 600i) on the cross-section of the sample at the interface between the coating and the substrate.

3. Results

3.1. Microstructures of the as-deposited coating

Fig. 1 shows the XRD patterns of the as-deposited Cr-CrN/TiSiN-Cr multilayer coating. Cubic CrN (c-CrN), cubic TiN (c-TiN), and cubic Cr (c-Cr) phases were detected in the coating. The c-Cr phase was the outer thin protective Cr coating. No clear peaks of Si and Si nitrides were observed due to the low content of these components in the coating. Fig. 2 depicts the fitted Cr 2p, Ti 2p, Si 2p, and N 1s XPS spectra of the as-deposited multilayer coating. The peaks in the Cr 2p spectrum were attributed to Cr and CrN phases (Fig. 2(a)). In the Ti 2p and Si 2p spectra, only peaks related to TiN and Si_3N_4 phases were obtained (Fig. 2(b) and (c)), respectively. The presence of these three types of nitrides can be verified by the N 1s XPS spectrum (Fig. 2(d)). Note that peaks corresponding to Cr—Ti or Ti—Si bonds inside the coating were not noticed. Based on the XRD (Fig. 1) and XPS results (Fig. 2), a total of four types of phases were present in the as-deposited coating: CrN, TiN, Si_3N_4, and Cr.

Fig. 3 shows the surface and cross-sectional microstructures of the as-deposited coating. The coating surface was smooth without cracks (Fig. 3(a) and (b)). However, a large number of particles and voids were distributed on the surface, which were also observed in other coatings fabricated by multi-arc ion plating [17,33,34]. Semi-quantitative elemental contents of these particles and the coating matrix at P1–P6 positions in Fig. 3(b) were evaluated by EDS point analysis, and the results are provided in Table 1. No significant differences were noticed between the element contents of the particles and the coating matrix, and mainly Cr and small amounts of Ti, Si, and N were present. As shown in the cross-section image of the as-deposited sample (Fig. 3(c)), the coating structure was consistent with the designed structure. According to the EDS line scans, Cr layers were distributed on both sides of the coating, and a CrN/TiSiN layer was dispersed in the middle of the coating. The coating was dense and tightly bonded to the Zircaloy substrate. The coating thickness was uniform, and the average thickness was measured to be ~15.2 μm. The average thickness of the Cr layers on both sides of the coating was ~1.2 μm. Nevertheless, microcracks parallel to the coating/substrate interface were distributed inside the nitride layer. Higher-magnification SEM image (Fig. 3(d)) demonstrated the presence of a superlattice structure inside the nitride layer, which was a nanoscale multilayer sequence of two different materials (with dark and bright colors). It can be clearly observed in Fig. 3(d) that the microcracks inside the nitride layer are distributed at the interface between nanolayers.

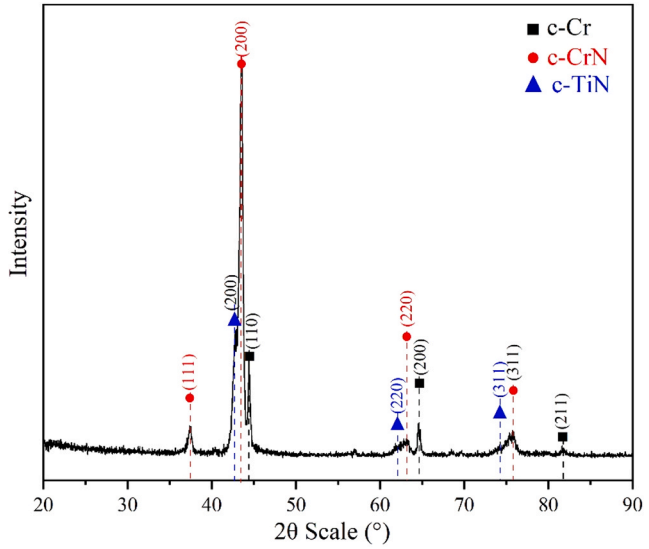

Fig. 1. XRD patterns of the as-deposited Cr-CrN/TiSiN-Cr coating.

To better study the microstructure of the middle CrN/TiSiN superlattice layer, further characterization was conducted using TEM, and the results are shown in Fig. 4. Fig. 4(a) depicts the high-angle annular dark field (HAADF) scanning transmission electron microscopy (STEM) image of the CrN/TiSiN superlattice layer; the superlattice structure was consistent with the SEM results (Fig. 3(d)). The structures of both the bright and the dark layers were continuous at the grain boundaries (Fig. 4(a)). Average thicknesses of the bright and dark layers were evaluated to be ~47.6 and ~31.2 nm, respectively. In the HAADF image, the brightness can be linked to the atomic number; thus, the bright layers should be CrN. Furthermore, according to the EDS maps (Fig. 4(b)), Cr and N were present in the bright layers, which confirmed that the bright layers were CrN layers. In contrast, Ti, Si, and N were distributed in the dark layers, indicating that the dark layers were TiSiN layers. Note that the concentration of N in the dark layers was higher than that in the bright layers because there were two types of nitrides (TiN and Si_3N_4) in the dark layers. Only a single cubic phase was identified via selected area electron diffraction (SAED) (Fig. 4(c)) by analyzing the diffraction rings, which implied the existence of a coherent lattice relationship between the CrN and TiN phases. However, no clear diffraction spots of the Si_3N_4 phase were obtained in the SAED pattern. This could be due to the fact that Si_3N_4 phase always exists as amorphous nanoparticles in Si-containing nitride coatings [17,35,36]. The amorphous phase can be observed by high-resolution TEM (HRTEM) in Fig. 4(f) inside the yellow circles, and the appearance of the amorphous phase can be further verified by the fast Fourier transform (FFT) pattern in Fig. 4(g) where there exists the halo ring pattern. This type of amorphous phase is possibly the Si_3N_4 amorphous nanoparticle. The grains of the CrN/TiSiN superlattice layer were columnar, as shown in the bright field (BF) image in Fig. 4(d) and the corresponding dark field (DF) image in Fig. 4(e). The HRTEM image of the CrN/TiSiN superlattice layer is shown in Fig. 4(h), and no clear phase boundaries were noticed between the CrN phase and the TiN phase, which further verified the coherent lattice relationship between these two phases.

3.2. Oxidation behavior of coated Zircaloy in steam

Fig. 5 shows the oxidation curves of weight gain versus time for Cr-CrN/TiSiN-Cr-coated and bare Zircaloy samples in steam at 1000 and 1200 °C. Images of the samples before and after oxidation are also depicted in Fig. 5. For steam oxidation at 1000 °C (Fig. 5(a)), the oxidation kinetics of the bare Zry-A tube initially obeyed a parabolic law, and then, a kinetic transition occurred at ~1200 s; finally, the weight gain rapidly increased with the oxidation time. The oxidation kinetics of Cr-CrN/TiSiN-Cr-coated Zry-A followed a parabolic law during the initial oxidation stage, and a kinetic transition took place at ~500 s. Nevertheless, even after the kinetic transition, the total weight gain of the coated sample (~1271.0 mg/dm^2) was substantially lower than that of the bare sample (~2967.7 mg/dm^2) after oxidation. As shown in Fig. 5(a), after exposure to steam at 1000 °C for 3600 s, most regions of the coated sample surface were appropriately protected; however, large cracks formed on the surface along the axial direction of the tube. Moreover, the edge of the tube was extensively attacked by steam. Therefore, it is highly possible that the oxidation of the edge and the formation of cracks led to the transition of the oxidation kinetics of the coated sample. During the entire oxidation process in steam at 1200 °C (Fig. 5(b)), the oxidation kinetics of bare Zry-4 obeyed a parabolic law. However, the oxidation kinetics of the coated sample at 1200 °C showed a similar variation to that at 1000 °C: a transition occurred at ~500 s, and then, the kinetics started following a faster exponential law instead of the parabolic law. The total weight gain of the coated sample (~3470.9 mg/dm^2) after oxidation was considerably lower than that of the bare Zry-4 sample (~7223.8 mg/dm^2). Surface morphology evolution during steam oxidation at 1200 °C was substantially different from that during steam oxidation at 1000 °C, and no evident cracks were observed on the surface of the rods; nevertheless,

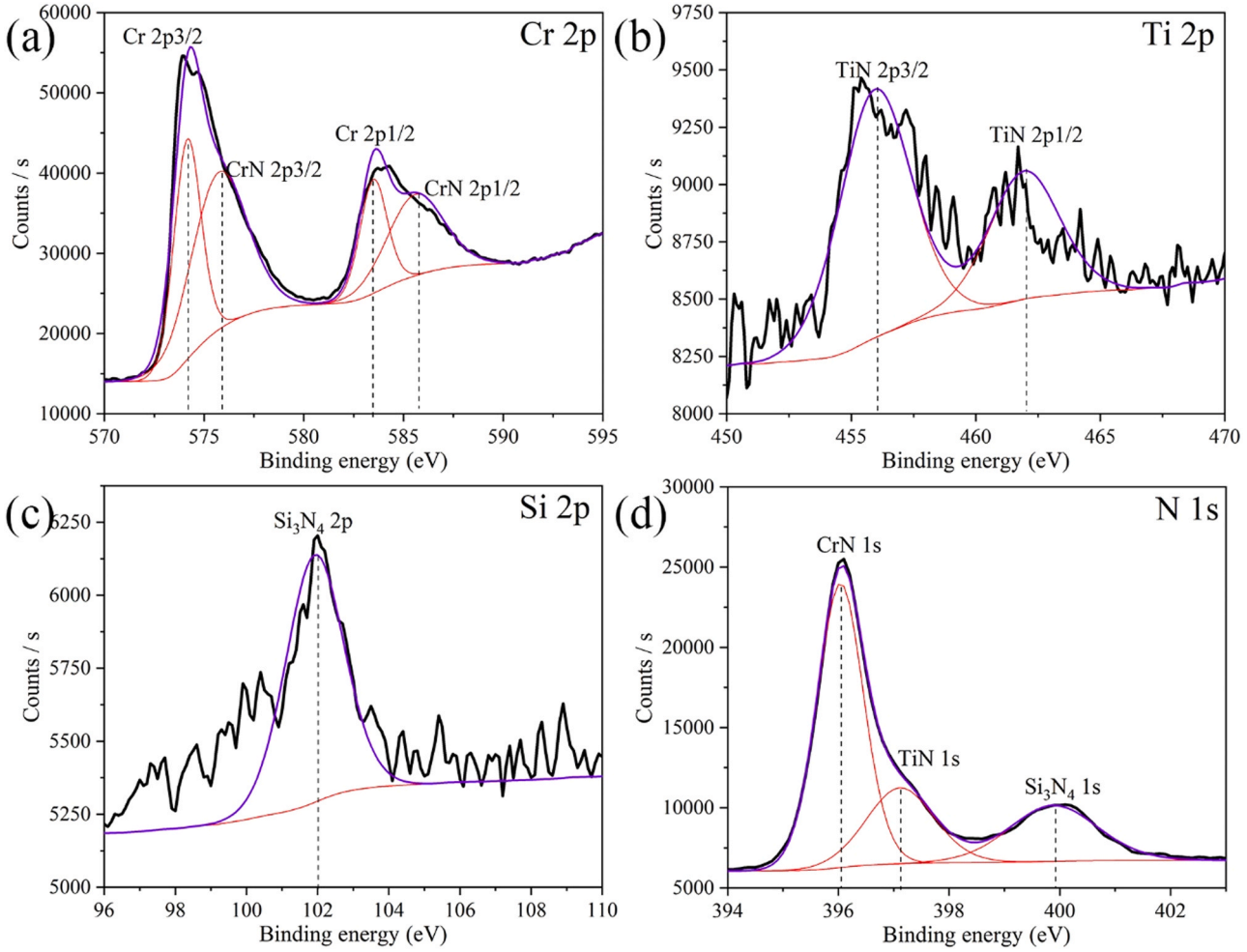

Fig. 2. Fitted (a) Cr 2p, (b) Ti 2p, (c) Si 2p, and (d) N 1s XPS spectra of the as-deposited Cr-CrN/TiSiN-Cr coating.

spallation occurred. Similar to the case of the tube sample, the corners of the rod samples significantly oxidized at 1200 °C. This phenomenon was primarily caused by stress concentration at the edges or the corners of the samples and was also noticed and discussed in our previous studies [16,17].

3.2.1. Microstructures of the samples after oxidation in steam at 1000 °C

Fig. 6 shows the surface microstructures of Cr-CrN/TiSiN-Cr-coated Zry-A after oxidation in steam at 1000 °C for 3600 s. At the edge of the coated Zry-A tube (Fig. 6(a)), circumferential and axial cracks were observed, and partial spallation of the coating occurred. Coating spallation and the formation of cracks could be the main reasons for the extensive oxidation of the edges. As shown in Fig. 6(b), microcracks and bulges formed on the surface of the coated sample after steam oxidation. According to the EDS maps (Fig. 6(d)), Ti was enriched at these bulges, which indicated outward diffusion of Ti through the outer Cr layer. Except for the bulge regions, most areas on the surface of the sample comprised Cr_2O_3. Based on the higher-magnification SEM image of the surface (Fig. 6(c)), the average grain size of Cr_2O_3 was ~160 nm. Small pores were distributed on the sample surface.

Fig. 7 depicts the cross-sectional microstructures of the coated tube after steam oxidation at 1000 °C for 3600 s. On the inner surface of the tube without coating, the Zircaloy substrate was seriously oxidized by steam. A thick non-protective oxide scale with an average thickness of ~172 μm generated after oxidation. However, on the coated outer surface of the tube, most regions of the substrate were suitably protected and not attacked by steam. Via the back-scattered electron SEM image (Fig. 7(b)) and EDS line scans (Fig. 7(d)), four layers were identified inside the coating after oxidation: an outermost Cr_2O_3 layer; a decomposing layer where no clear elemental distribution differences were observed, since the superlattice structure of this layer was destroyed (Fig. 7(c)); a middle unoxidized CrN/TiSiN coating layer, whose superlattice structure was maintained (Fig. 7(c)); and an innermost Cr interlayer. The average thickness of the Cr_2O_3 scale was ~2 μm, which suggested that this oxide scale was primarily the oxidation product of the original outer Cr layer (~1.2 μm) due to the large Pilling–Bedworth ratio (PBR, ~2 [37]) during the oxidation of Cr. Inside the decomposing layer beneath the oxide scale (Fig. 7(c)), the TiSiN nanolayers between CrN layers transformed into pores, which indicated the decomposition of TiSiN. Considering the appearance of Ti precipitates on the surface of the sample (Fig. 6(b)), this decomposition may be attributed to outward diffusion of Ti. The average thickness of the Cr interlayer was 0.7 μm, which was substantially lower than that of the original outer Cr layer (1.2 μm). Note that a Zr–Cr intermetallic compound layer formed between the Cr interlayer and the Zircaloy substrate. The presence of Zr inside the nitride coating was verified by EDS line scans (Fig. 7(d)).

3.2.2. Surface phases of the coating after oxidation in steam at 1200 °C

Fig. 8 presents the XRD patterns of the Cr-CrN/TiSiN-Cr coating after steam oxidation at 1200 °C for 1500 s and 3600 s. No diffraction peaks of the original nitride coating were noticed owing to the formation of a thick oxide scale on the surface of the coating after oxidation. After oxidation at 1200 °C for 1500 s, four types of oxide phases formed on the surface of the sample: $(Cr_{1-x}Ti_x)_2O_3$ (x was close to 0.12 based on the

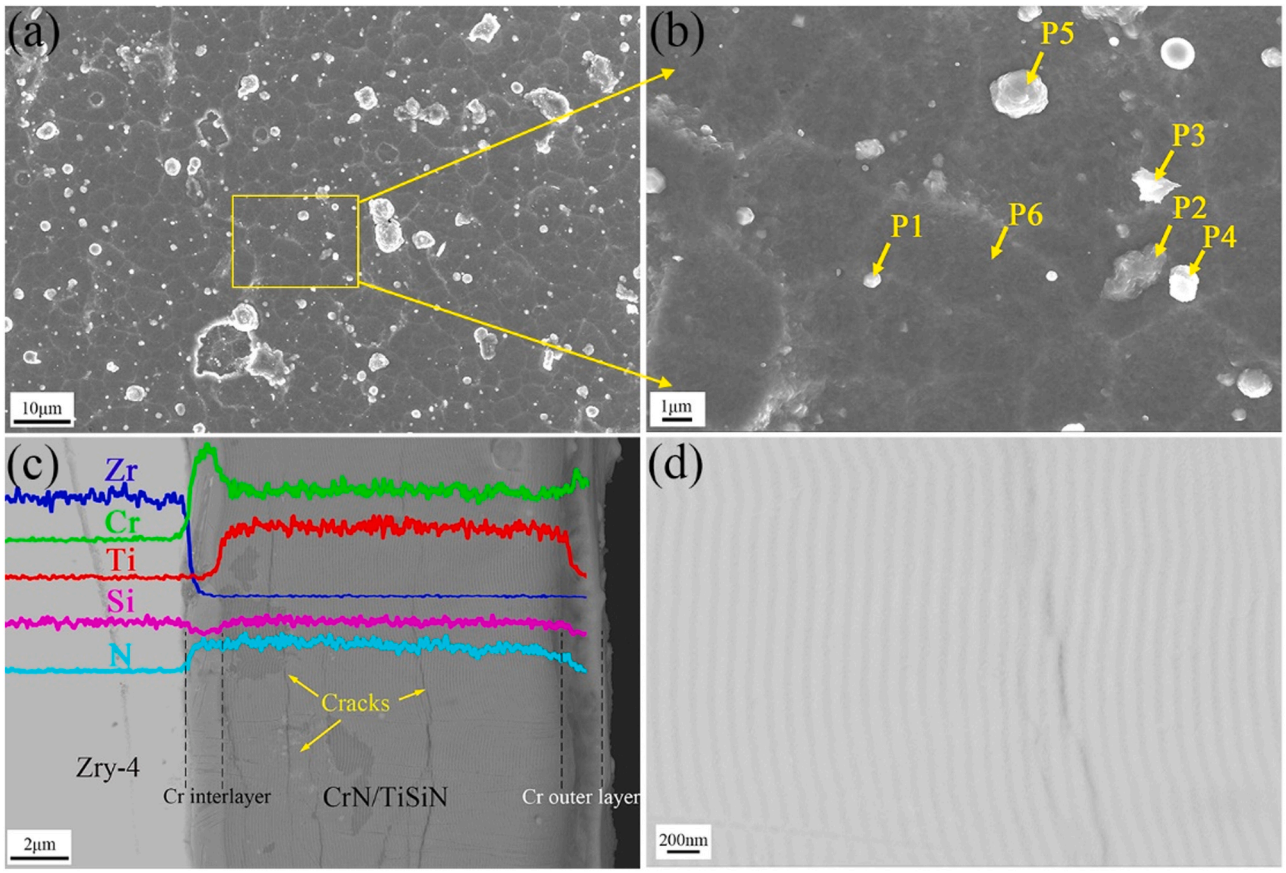

Fig. 3. SEM images of the as-deposited Cr-CrN/TiSiN-Cr coating: (a) surface at low magnification, (b) surface at high magnification, (c) cross-sectional microstructure at low magnification along with EDS line scans, and (d) cross-sectional microstructure at high magnification.

Table 1
The semi-quantitative elemental contents at P1–P6 positions in Fig. 3(b).

at%	P1	P2	P3	P4	P5	P6
Cr	82	86	89	79	88	87
Ti	7	7	3	5	4	4
Si	0	0	0	1	0	0
N	11	7	8	15	8	9

positions of diffraction peaks), Cr_2TiO_5, ZrO_2, and SiO_2. The $(Cr_{1-x}Ti_x)_2O_3$ phase was generated due to the substitution of partial Cr atoms in the Cr_2O_3 grains by Ti atoms. Owing to the larger atomic volume of Ti when compared with that of Cr, the lattice parameters of the $(Cr_{1-x}Ti_x)_2O_3$ phase (a 4.97217 Å, b 4.97217 Å, and c 13.6343 Å when x 0.12 (namely, the $(Cr_{0.88}Ti_{0.12})_2O_3$ phase)) were larger than those of the Cr_2O_3 phase (a 4.95876 Å, b 4.95876 Å, and c 13.5942 Å). The Cr_2TiO_5 phase had also formed during the oxidation of Cr- and Ti-containing MAX ceramics [38]. In addition, a similar stoichiometric oxide phase of Al and Ti (that is, Al_2TiO_5 phase) was produced after the oxidation of a TiAlN coating in air [39]. The formation of the ZrO_2 phase can be ascribed to two factors: 1) spallation of the surface coating and oxidation of the Zircaloy substrate and 2) outward diffusion of Zr through the coating followed by further oxidation inside the coating, which has been extensively observed and studied during the oxidation of Cr coatings on Zircaloy substrates [15,19]. The SiO_2 phase could be the oxidation product of Si_3N_4 in the coating. These four oxide phases were also noticed on the surface of the sample exposed to steam at 1200 °C for 3600 s. However, a small difference was found between these two samples with different oxidation times: leftward shifts of the diffraction peaks of $(Cr_{1-x}Ti_x)_2O_3$ and Cr_2TiO_5 phases occurred in the case of the sample with an oxidation time of 3600 s. Note that such peak shifts were not caused by the effects of stress inside the oxide scale because there was no change in the positions of the peaks of ZrO_2 and SiO_2 phases. Consequently, it should have been induced by an increase in the lattice parameter according to the Bragg equation. This indicated that more Ti atoms were doped into the lattices of the $(Cr_{1-x}Ti_x)_2O_3$ and Cr_2TiO_5 phases. To differentiate the Ti contents, $(Cr_{1-y}Ti_y)_2O_3$ ($y > x$) and $(Cr_{1-z}Ti_z)_2TiO_5$ were employed to describe the abovementioned two phases after oxidation for 3600 s. The TiO_2 phase, which is the primary oxidation product of Ti-containing nitride coatings or ceramics [40–42], was not observed on the surfaces of the samples after oxidation.

3.2.3. Microstructures of the sample after oxidation in steam at 1200 °C for 1500 s

Fig. 9 depicts the surface and cross-sectional SEM images of Cr-CrN/TiSiN-Cr-coated Zry-4 after oxidation in steam at 1200 °C for 1500 s. As shown in Fig. 9(a), the surface of the sample after oxidation was relatively smooth, and no significant cracks were noticed on it. Although the oxide grains on the surface were relatively small, a few large needle-like grains were distributed on the surface. According to the EDS maps (Fig. 9(b)), mainly Cr, Ti, and O were distributed on the surface, and small amounts of Si, N, and Zr were also observed. No elemental segregation was detected on the surface. Oxidation of the Zry-4 substrate was appropriately prevented by the surface coating, as observed from the cross-section image shown in Fig. 9(c). After oxidation, the coating was dense without cracks. However, pores formed at the interface between the mixed oxide layer and the unoxidized nitride coating. In local regions of the sample (Fig. 9(f)), these pores connected to each other, and a large crack was generated at the oxide/nitride coating interface,

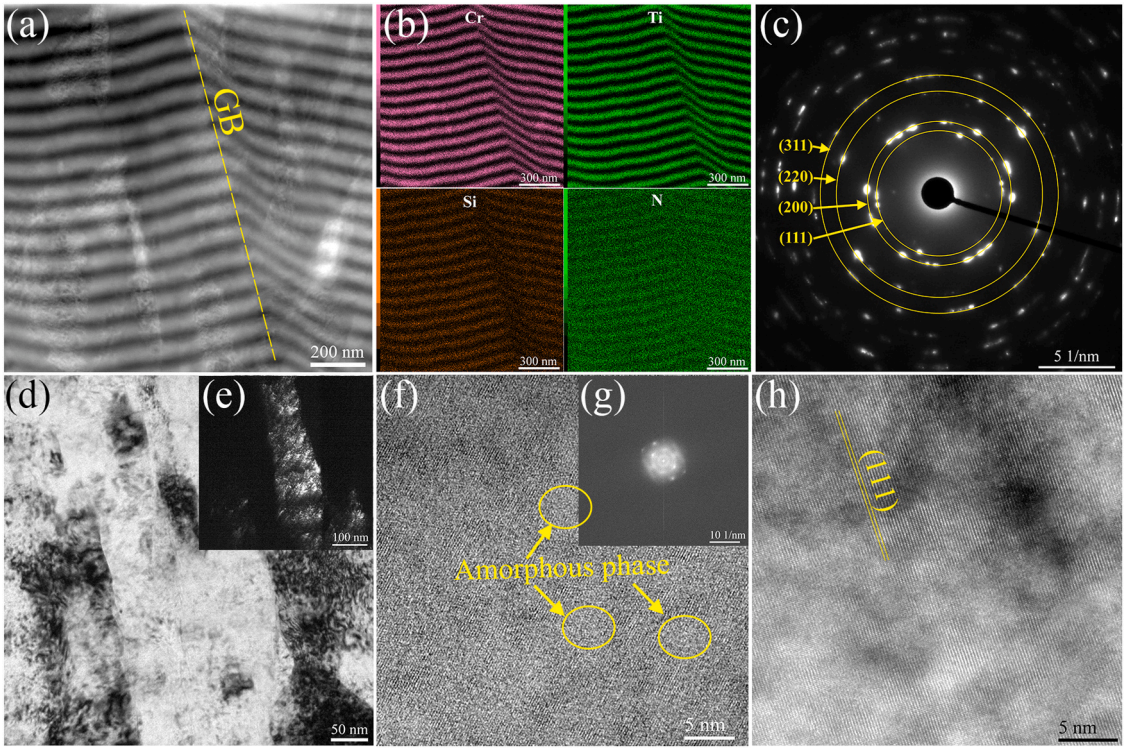

Fig. 4. TEM characterization of the as-deposited CrN/TiSiN superlattice layer: (a) HAADF-STEM image, (b) EDS maps of (a), (c) SAED pattern, (d) BF-TEM image, (e) DF-TEM image of (d), (f) HRTEM image of the TiSiN layer, (g) FFT pattern of (f), and (h) HRTEM image. GB: Grain boundary.

which separated the outer mixed oxide layer from the coating matrix. After exposure to steam at 1200 °C for 1500 s, the coating was not completely consumed by oxidation. A multilayer structure formed inside the coating, and the layers, from the outside to the inside, were identified as a Cr-rich mixed oxide layer, a Ti-rich mixed oxide layer, a Cr-rich mixed oxide layer, an unoxidized nitride coating, and a Cr interlayer, respectively, by the EDS maps (Fig. 9(d)) and EDS line scans (Fig. 9(e)). The EDS maps (Fig. 9(d)) indicated a Ti concentration gradient inside the middle Cr-rich mixed oxide layer, and Ti segregation was noticed at the oxide/nitride coating interface. Si segregated on the surface of the sample after oxidation. A Si-rich layer was also observed at the oxide/nitride coating interface. Nevertheless, this Si-rich layer was formed by the filling of the SiO_2 polishing paste in the pores at the interface during sample polishing instead of by the segregation of Si. Note that Zr was found inside the coating, which implied that Zr in the substrate diffused outward into the coating. A Zr–Cr layer was also discovered at the coating/substrate interface via the EDS line scans (Fig. 9(e)). Partial spallation of the outermost Cr-rich mixed oxide layer is shown in Fig. 9(c). However, in local regions of the coating (Fig. 9(f)), the entire Cr-rich mixed oxide layer and some of the inner Ti-rich mixed oxide layer peeled. This result is consistent with the image of the sample surface in Fig. 5(b), showing spallation of the local dark oxide layer. Fig. 9(g) presents the microstructure of the oxide/nitride coating interface. On the nitride coating side, dark Ti segregated close to the interface, and in these regions, the coating no longer had the superlattice structure. In contrast, the superlattice structure inside the nitride coating far from the interface was not destroyed after oxidation.

3.2.4. *Microstructure after oxidation in steam at 1200 °C for 3600 s*

Fig. 10 shows the surface morphologies of the Cr-CrN/TiSiN-Cr coating after oxidation in steam at 1200 °C for 3600 s. The surface was no longer smooth, and large bulges (indicated by yellow arrows) and small precipitates (shown by blue arrows) were distributed on it. The appearance of these small precipitates was similar to that of the Ti-rich precipitates observed on the surface of the sample after oxidation at 1000 °C (Fig. 6(b)). However, the EDS maps (Fig. 10(b)) indicated no Ti segregation inside these precipitates. Moreover, no clear elemental segregations were detected at the positions of the large bulges. The elements on the surface of the sample were mainly Cr, Ti, and O. Small amounts of Zr, N, and Si were also observed on the surface. As shown in the higher-magnification SEM image (Fig. 10(c)), the grain size of the surface oxide was larger than those of the samples after oxidation at 1200 and 1000 °C for 1500 s and 3600 s, respectively. According to the EDS maps (Fig. 10(d)), the surface oxides with large grains were primarily the mixed oxides of Cr and Ti. Interestingly, small ZrO_2 grains were identified via the EDS maps. These ZrO_2 grains were distributed not only at the grain boundaries of the mixed oxide (indicated by yellow arrows), but also inside the grains of the mixed oxide (shown by blue arrows).

Fig. 11 shows the cross-sectional microstructures of the samples exposed to steam at 1200 °C for 3600 s. The microstructures of the samples exposed to steam at 1200 °C for 1500 s and 3600 s were considerably different; however, there were also some similarities. The coating was completely consumed with no nitride layer, and the superlattice structure was destroyed. Layers from the outside to the inside of the multilayer structure (Fig. 11(a)) were determined to be a Cr–Ti mixed oxide layer, a Cr-rich mixed oxide layer, a Ti-rich mixed oxide layer, and a Cr interlayer, respectively, via the EDS maps (Fig. 11(b)) and line scans (Fig. 11(c)). A Zr–Cr layer formed between the coating and the substrate after oxidation. In the Cr–Ti mixed oxide layer, the ratio of the concentrations (at%) of Cr and Ti was close to 1. Small dark precipitates were dispersed close to the outer surface of the sample (indicated by white arrows), whose microstructures were similar to those of the Ti-rich precipitates beneath the outermost Cr-rich layer in the sample exposed to steam oxidation for 1500 s (Fig. 9(c)). Note that the thickness of the Cr interlayer was higher when compared with that in the case of the sample exposed to steam oxidation for 1500 s. In most regions of the sample, no continuous porous layers were detected inside the coating. The pores, which formed after oxidation at 1200 °C for 1500 s, at the oxide/nitride coating interface entirely disappeared after

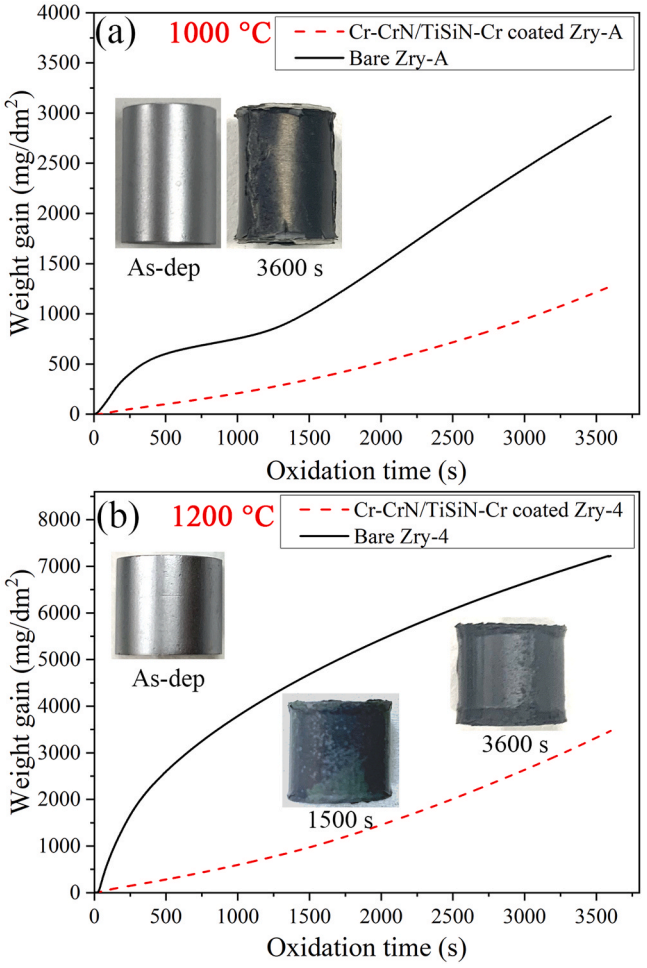

Fig. 5. Isothermal oxidation kinetics of the bare and coated Zircaloy samples along with the surface images of the coated samples before and after oxidation: (a) oxidation in steam at 1000 °C for 3600 s and (b) oxidation in steam at 1200 °C for 3600 s.

further oxidation for 3600 s. Nevertheless, in local regions of the sample, large cracks were generated inside the coating; these cracks were parallel to the coating/substrate interface and separated the mixed oxide layer and the unoxidized coating (Fig. 11(d)). These regions with large cracks were associated with the bulges observed on the surface of the sample (Fig. 10(a)). Interestingly, the EDS maps (Fig. 11(f)) indicated that the single Cr_2O_3 phase precipitated in the mixed oxide layer outside the bulges (Fig. 11(e)).

4. Discussion

4.1. Microstructure of the as-deposited coating

The middle CrN/TiSiN layer inside the as-deposited multilayer coating had a superlattice structure composed of a nanoscale multilayer sequence of CrN/TiSiN. Inside the TiSiN layers, nano-sized Si_3N_4 particles possibly dispersed in the TiN matrix; however, no Ti–Si bonds were produced. A coherent lattice relationship, which is typically the primary characteristic of a superlattice structural coating [28,43,44], existed between the CrN and TiN layers. Both TiN and CrN have face-centered cubic (fcc) structures and B1 lattice structures. Only a small difference was noticed between the lattice parameters of CrN (a b c 0.4148 nm) and TiN (a b c 0.4241 nm), and the lattice misfit of crystal orientation between CrN and TiN was calculated to be 2.2%. Superlattice structure improves the thermal stability of the coating [29,45,46], and, in this study, the unoxidized coating can maintain the nitride superlattice structure at 1000 °C and 1200 °C. However, cracks were distributed along the CrN/TiSiN interface. The formation of cracks may be attributed to the small lattice mismatch between TiN and CrN.

4.2. Oxidation behavior and oxidation mechanism of the as-deposited multilayer coating on Zircaloy substrates

Oxidation behavior of the Cr-CrN/TiSiN-Cr-coated Zircaloy at high temperatures is complicated owing to the complex structure and multi-element nature of this surface coating and the interdiffusion behavior between the coating and the substrate. Fig. 12 depicts the schematics describing the oxidation behavior and oxidation mechanism of the Cr-CrN/TiSiN-Cr-coated Zircaloy. The microstructure of the as-deposited coating is shown in Fig. 12(a). At the initial stage of oxidation (Fig. 12 (b)), a single-phase Cr_2O_3 scale formed by the reaction between steam and the outer Cr layer (Fig. 7(b)) as follows:

$$2Cr + 3H_2O \rightarrow Cr_2O_3 + 3H_2 \quad (1)$$

This kind of oxidation is mainly dominated by the outward diffusion of Cr cations [47,48] when only one type of cations exists during oxidation; nevertheless, Ti, Si, and Zr also diffused from the inner superlattice coating and substrate to the outer surface of the coating (Fig. 6(d) and 7(d)), respectively. This outward diffusion of other elements can affect the oxidation behavior of Cr. Therefore, the inward diffusion of O during this type of oxidation cannot be ignored. Furthermore, inward diffusion of O was reported during the oxidation of the TiCrN coating [49]. After the Cr outer layer was consumed, oxidation of the inner superlattice coating occurred. Accordingly, the oxidation behaviors of multi-element coatings should depend on the O affinities of all components. Standard Gibbs formation energies ($\triangle G_f$) of several oxides (per mol O_2) at 1000 and 1200 °C are presented in Table 2. According to the $\triangle G_f$ values of different oxides, the O affinities of Cr, Ti, Si, and Zr are in the following order: Zr > Ti > Si > Cr. Therefore, during the oxidation of the CrN/TiSiN superlattice coating, the oxidation of Ti and Si preceded the oxidation of Cr. Outward diffusions of Ti, Si, and Zr took place due to the O potential gradient, which extended from the gas/coating interface to the substrate [50]. Moreover, the decomposition of the TiSiN layer occurred before the decomposition of the CrN layer, which was the primary reason for the formation of the decomposing layer beneath Cr_2O_3 and the appearance of pores at the position of the TiSiN layer (Fig. 7(c)). Schematics of the decomposition of the superlattice CrN/TiSiN layers are shown in Fig. 13, and the N atoms are not depicted in these schematics. Outward diffusion of Ti atoms led to the production of vacancies at the original positions of the Ti atoms (Fig. 13(b)). Subsequently, with the further outward diffusion of Ti, more vacancies formed. These vacancies coalesced with each other, eventually resulting in the production of pores inside the TiSiN layer (Fig. 13(c)). Note that these pores can act as sinks for absorbing N_2 generated during the decomposition and oxidation of the nitride coating [16,17]. As shown in Fig. 12(b), in local regions, Ti reached the outer surface of the coating and formed Ti-rich oxides, which was the reason for the appearance of Ti precipitates (Fig. 6(b)). As shown in the image of the surface (Fig. 6(b)), microcracks that penetrated through these precipitates were always generated. Therefore, the inhomogeneous outward diffusion of Ti atoms and the formation of precipitates on the surface may have led to changes in the surface stress and the production of microcracks. At the Cr interlayer/Zircaloy substrate interface, interdiffusion and solid reactions occurred between Zr and Cr; thus, the thickness of the Cr interlayer decreased, and a Zr–Cr layer formed beneath the Cr interlayer. This type of Zr–Cr layer has always been observed during the high-temperature oxidation of Cr-coated Zircaloy [15,19,22].

Theoretically, the oxidation of TiN is mainly controlled by the

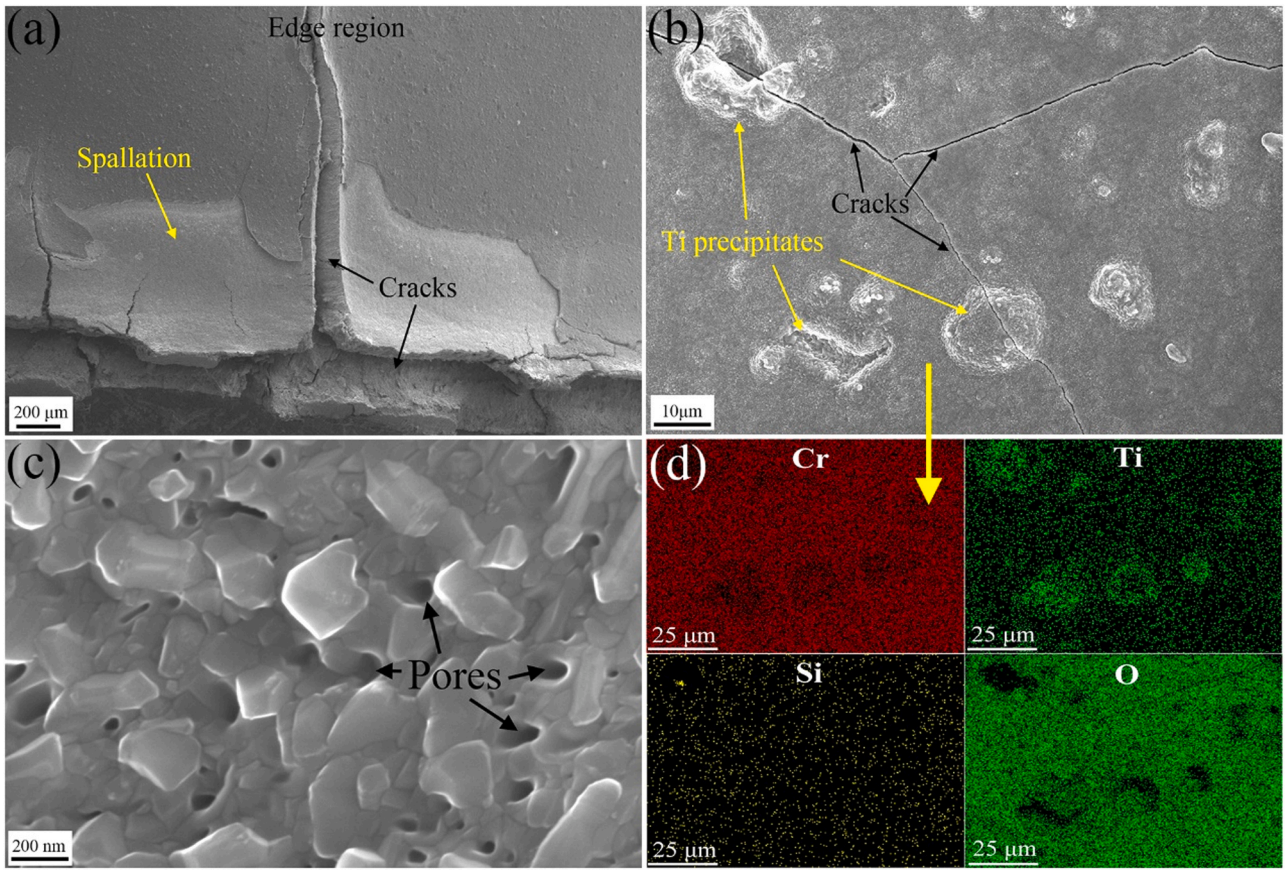

Fig. 6. Surface SEM characterization of the Cr-CrN/TiSiN-Cr-coated Zry-A tube after oxidation in steam at 1000 °C for 3600 s: (a) edge of the tube, (b) surface microstructure at low magnification, (c) surface microstructure at high magnification, and (d) EDS maps of (b).

inward diffusion of O through the oxide layer [51]. However, in this study, the oxidation mechanism was significantly different. As shown in Fig. 12(c), when Ti diffused into the outer Cr_2O_3 layer, the Cr atoms in Cr_2O_3 were replaced by Ti atoms because of the higher O affinity of Ti than that of Cr. Therefore, the outer oxide phase transformed into a $(Cr_{1-x}Ti_x)_2O_3$ phase via the reaction described in Eq. 2. This $(Cr_{1-x}Ti_x)_2O_3$ layer is the outermost Cr-rich layer shown in Fig. 9(c).

$$2x\mathrm{TiN} + \mathrm{Cr_2O_3} \rightarrow (\mathrm{Cr_{1-x}Ti_x})_2\mathrm{O_3} + 2x\mathrm{Cr} + 2x\mathrm{N} \quad (2)$$

Beneath the $(Cr_{1-x}Ti_x)_2O_3$ layer, CrN and TiN were oxidized by the inward diffused O, and a mixed oxide (Cr_2TiO_5) layer formed via the reaction presented in Eq. 3. This Cr_2TiO_5 layer is the middle Ti-rich mixed oxide layer depicted in Fig. 9(c), and the concentration of Ti in the Cr_2TiO_5 layer was substantially higher than that in the $(Cr_{1-x}Ti_x)_2O_3$ layer.

$$\mathrm{TiN} + 2\mathrm{CrN} + 5\mathrm{O} \rightarrow \mathrm{Cr_2TiO_5} + 3\mathrm{N} \quad (3)$$

With the fast outward diffusion of Ti, a large number of CrN molecules were left below the Cr_2TiO_5 outer layer. Thereafter, these CrN molecules were further oxidized by the inward diffused O, and a thick Cr-rich mixed oxide layer was produced. Moreover, the nitride coating beneath this Cr-rich oxide layer continued to decompose, and Ti continuously diffused outward to this Cr-rich oxide layer and replaced the Cr atoms in Cr_2O_3. This is the reason for the development of a Ti concentration gradient inside the Cr-rich oxide layer and the segregation of Ti in the nitride coating close to the oxide/nitride coating interface. During the oxidation of the inner superlattice coating, the oxidation behavior was primarily controlled by the outward diffusion of Ti and inward diffusion of O, which was also detected during the oxidation of the TiCrN coating [52]. The outward diffusion of Cr may be inhibited by the outward diffusions of Ti, Zr, and Si, whose O affinities are higher than that of Cr. During oxidation, a SiO_2 layer generated close to the surface of the coating, which was the oxidation product of outwardly diffused Si and inwardly diffused O. Zr in the substrate also diffused into the coating. When numerous Ti atoms diffused to the outer surface of the coating and uniformly dispersed on the coating surface, almost no elemental difference was noticed between the original Ti precipitates and the mixed oxide matrix (Fig. 10(b)). In this oxidation stage, a porous layer formed at the oxide/nitride coating interface. There are two possible mechanisms for the formation of interfacial pores: 1) the pores produced by the outward diffusion of Ti and the decomposition of the TiSiN layer (Fig. 13(c)) further absorb vacancies and N_2 and grow, and 2) Kirkendall voids generated owing to the difference between the diffusion coefficients of Ti and Cr during oxidation [53].

With an increase in the oxidation time, the further outward diffusion of Ti transformed the $(Cr_{1-x}Ti_x)_2O_3$ and Cr_2TiO_5 phases to $(Cr_{1-y}Ti_y)_2O_3$ ($y > x$, ~1) and $(Cr_{1-z}Ti_z)_2TiO_5$ phases due to the replacement of the Cr atoms in the crystal lattice by Ti atoms (Fig. 12(d)). This transformation led to a leftward shift of the XRD peaks of these two phases (Fig. 8). The thickness of the $(Cr_{1-y}Ti_y)_2O_3$ layer (the outermost Cr-Ti oxide layer in Fig. 11(a)) increased owing to the outward diffusion of Ti. Correspondingly, the thickness of the Cr-rich mixed oxide layer beneath the $(Cr_{1-y}Ti_y)_2O_3$ outer layer (Fig. 11(a)) decreased as compared to that of the Cr-rich layer (Fig. 9(c)). However, the thickness of the $(Cr_{1-z}Ti_z)_2TiO_5$ layer significantly decreased and only a few particles remained close to the surface after oxidation. This decrease in the content of the $(Cr_{1-z}Ti_z)_2TiO_5$ phase was also indicated by the XRD patterns shown in Fig. 8. This content reduction may be due to the instability of the Cr_2TiO_5 phase at high temperatures and its decomposition during oxidation [54]. During the oxidation of the remaining unoxidized superlattice coating, Ti diffuses outward and is preferentially oxidized

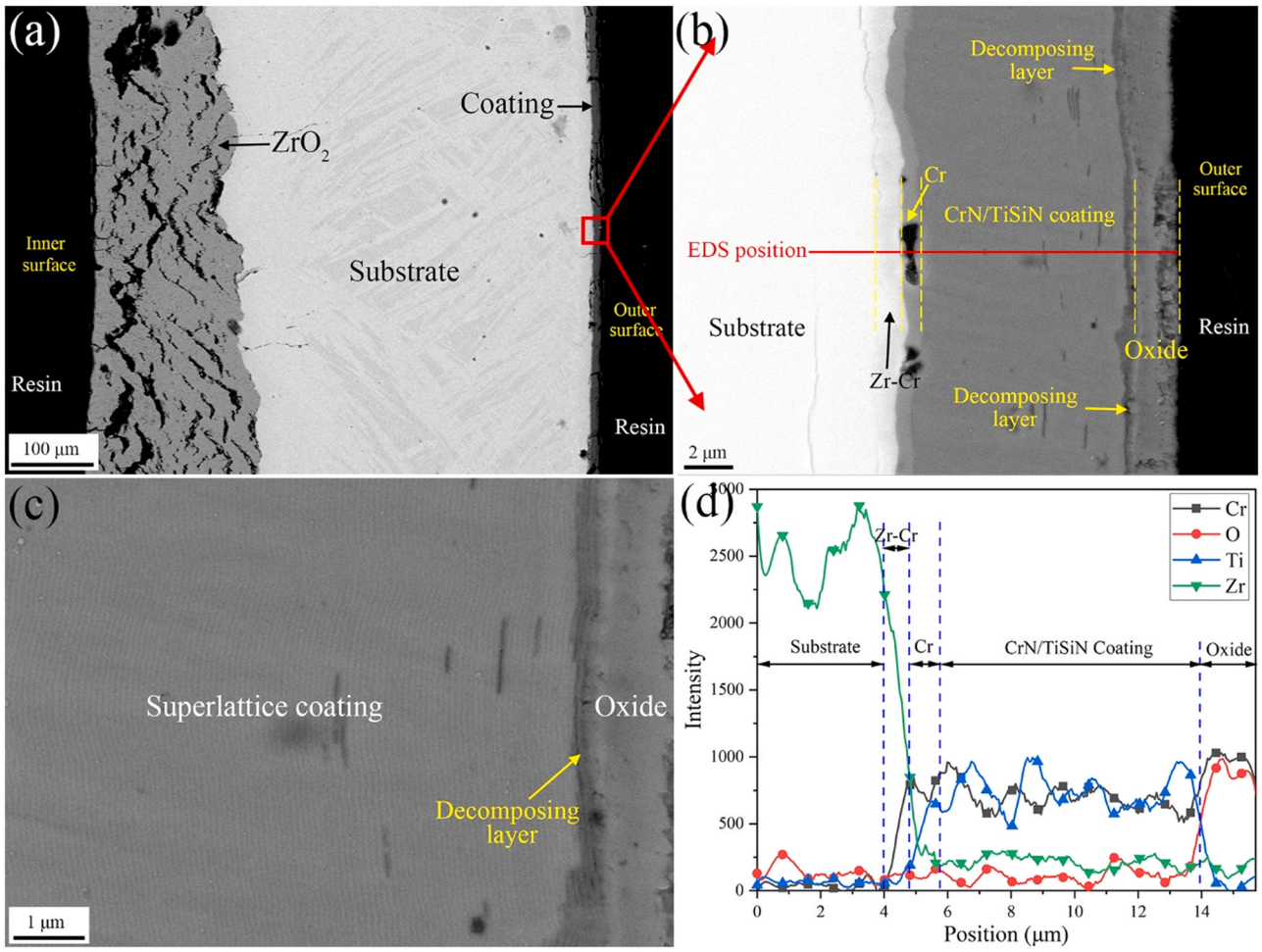

Fig. 7. Cross-sectional SEM characterization of the Cr-CrN/TiSiN-Cr-coated Zry-A tube after oxidation in steam at 1000 °C for 3600 s: (a) SEM image at low magnification, (b) SEM image at high magnification; (c) SEM image of the middle superlattice nitride coating; and (d) EDS line scans of (b).

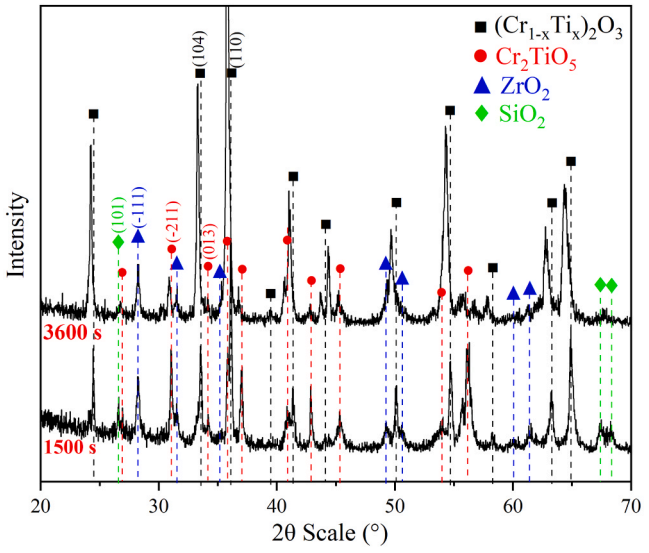

Fig. 8. XRD patterns of the Cr-CrN/TiSiN-Cr coating after steam oxidation at 1200 °C.

by O that diffuses inward; thus, a Ti-rich mixed oxide forms. Furthermore, CrN is left inside the coating close to the Cr interlayer. Because of the instability of CrN [16], CrN further decomposes into Cr. This part of Cr increases the thickness of the Cr interlayer and diffuses inward to the Zircaloy substrate owing to the large diffusion coefficient and solubility of Cr in Zr [15,22], which has been extensively reported during the high-temperature oxidation of Cr-coated Zircaloy substrate systems [15, 19]. This oxidation of Ti and Cr beneath the original oxide/nitride coating interface (Fig. 12(c)) results in volume expansion due to the large PBR during the generation of oxides, which further fills the pores at the oxide/nitride coating interface. This is the reason for the complete disappearance of the original pores at the oxide/nitride interface when the material was oxidized for a longer time (Fig. 12(a)). Nevertheless, in local regions of the coating (Fig. 12(d)), the pores at the oxide/nitride interface did not disappear; instead, they further absorbed N_2 and eventually developed into bulges, which entirely separated the oxide and the coating matrix (Fig. 11(d)). Such bulges further caused the formation of cracks inside the coating and the spallation of the oxide scale. In this case, the outward diffusion of Ti from the nitride matrix to the outer oxide layer was completely suppressed by the bulges. However, Ti inside the outer mixed oxide layer continued to diffuse outward to the outer surface of the coating. Therefore, the single Cr_2O_3 phase precipitated inside the mixed oxide layer outside the bulges owing to the loss of Ti. N_2 produced by the decomposition and oxidation of the nitride coating not only diffused outward and generated bulges, but also diffused inward and produced pores inside the Cr interlayer. During oxidation, a large amount of Zr diffused to the outer surface of the coating through both the grain boundaries and the bulk of the mixed oxides, which suggested that the mixed oxides formed by oxidation and the multilayer coating could not act as effective barriers to the diffusion

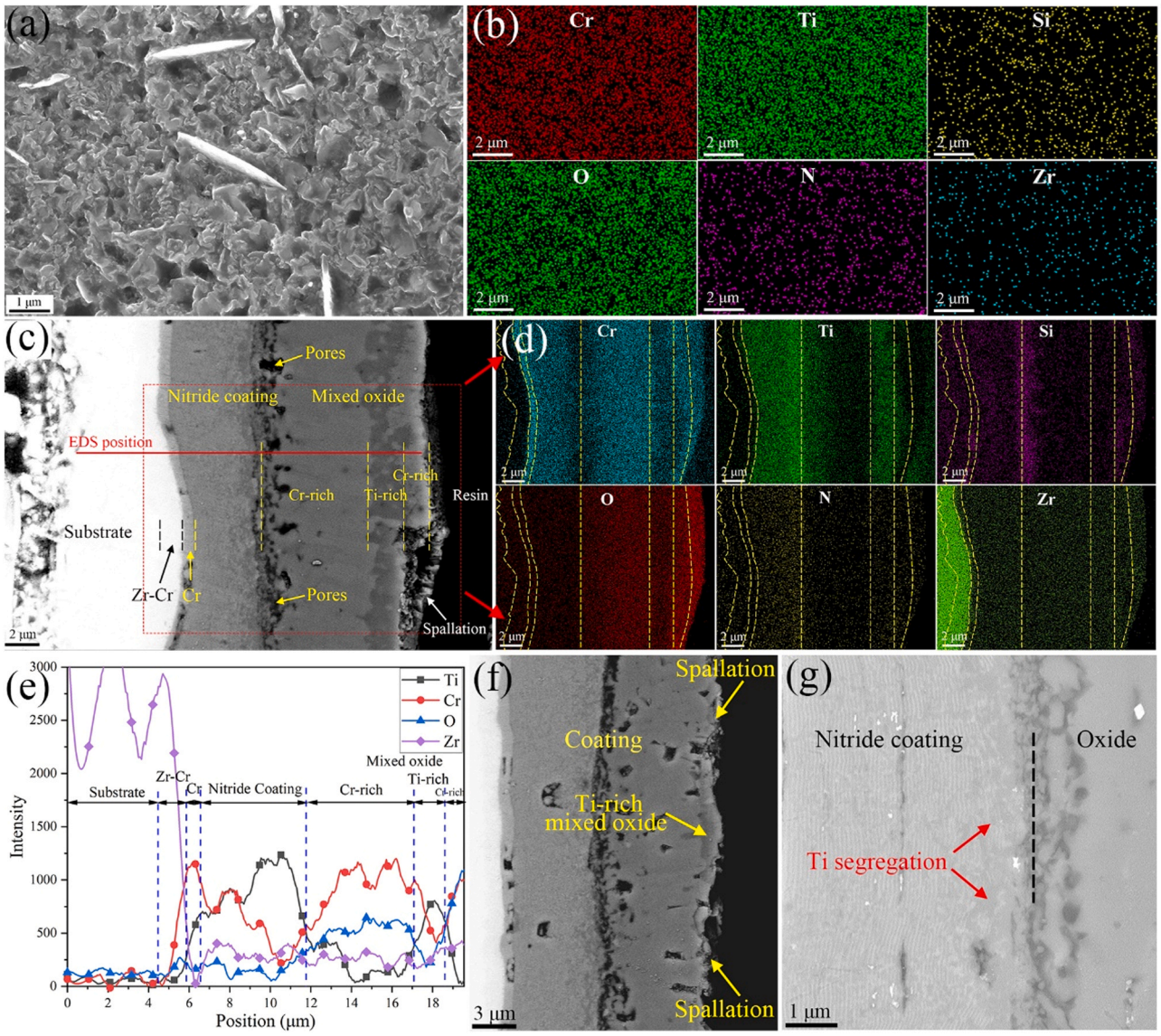

Fig. 9. Surface and cross-sectional SEM characterization of the Cr-CrN/TiSiN-Cr coated Zry-4 rod after oxidation in steam at 1200 °C for 1500 s: (a) surface SEM image, (b) EDS maps of (a), (c) cross-sectional SEM image, (d) EDS maps of the local region in (c), (e) EDS line scans of (c), (f) cross-sectional SEM image of the region with surface spallation, and (g) cross-sectional SEM image at the oxide/nitride coating interface.

of Zr.

The degradation of the multilayer coating on Zircaloy substrates will occur if exposure in steam atmosphere at 1200 °C for a longer time (> 3600 s) according to the oxidation behavior and oxidation mechanism discussed above. There are mainly three reasons that will cause the failure of the surface coating:

1) The formation of bulge will lead to the spallation of oxide scale and surface coating. Moreover, the bulge can cause the formation of cracks inside the coating (Fig. 10(a)).
2) The mixed oxide formed during the oxidation cannot effectively block the outward diffusion of Zr. Similar with the oxidation of Cr coating-Zircaloy substrate [15], the outward diffusion and oxidation of Zr can significantly affect the oxidation of coating and accelerate the failure of the surface coating.
3) The formation of pores inside the coating due to the release of N during the oxidation is a factor that can affect the structural integrity of coating [16,17].

5. Conclusion

In this study, Cr-CrN/TiSiN-Cr multilayer coatings were deposited on Zircaloy tubes and solid rods. Microstructures of the as-deposited coatings, specifically those of the CrN/TiSiN superlattice layers, were comprehensively analyzed. Oxidation behaviors of the multilayer coatings under a steam atmosphere at 1000 and 1200 °C were investigated. Oxidation mechanisms of the coatings, particularly those of the CrN/TiSiN superlattice layers, were discussed. The following conclusions were drawn from the results obtained in this study:

(1) The microstructure of the CrN/TiSiN superlattice layer in the as-deposited multilayer coating was composed of nanoscale multilayer sequences of CrN (~47.6 nm) and TiSiN (~31.2 nm). A coherent lattice relationship existed between the CrN and TiSiN layers. In the TiSiN layer, nanosized Si_3N_4 particles were dispersed in the TiN matrix.
(2) The surface multilayer coating improved the oxidation resistance of the Zircaloy substrate in steam at 1000 and 1200 °C within 3600 s. Oxidation behavior of the nitride coating was controlled

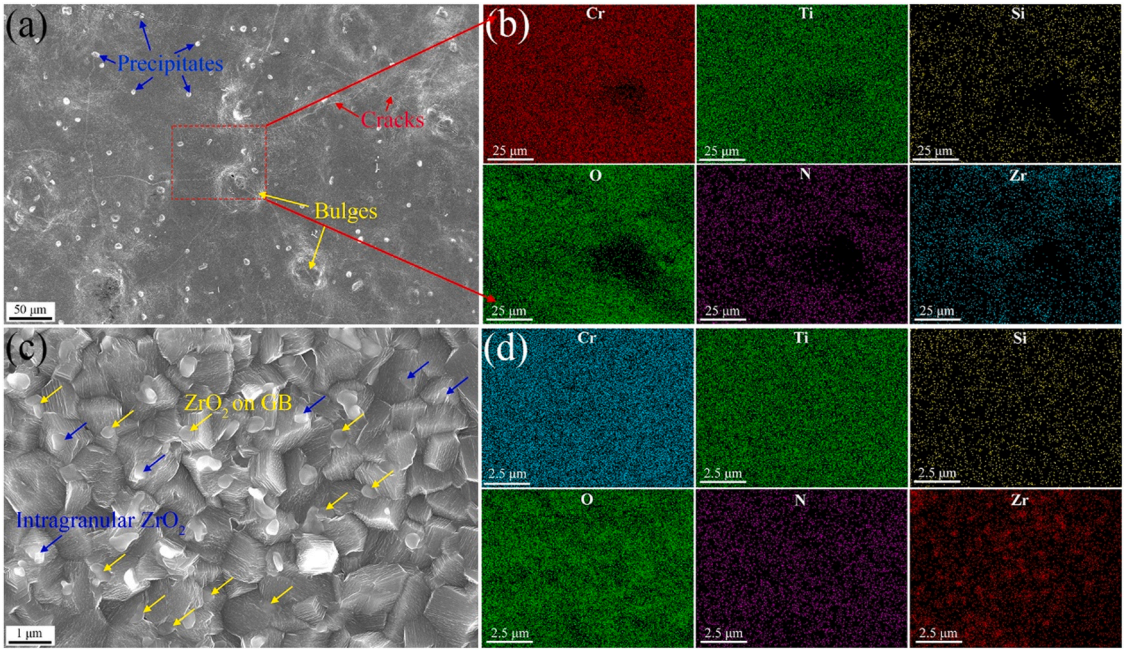

Fig. 10. Surface SEM characterization of the Cr-CrN/TiSiN-Cr-coated Zry-4 rod after oxidation in steam at 1200 °C for 3600 s: (a) surface microstructure at low magnification, (b) EDS maps of (a), (c) surface microstructure at high magnification, and (d) EDS maps of (c). GB: grain boundary.

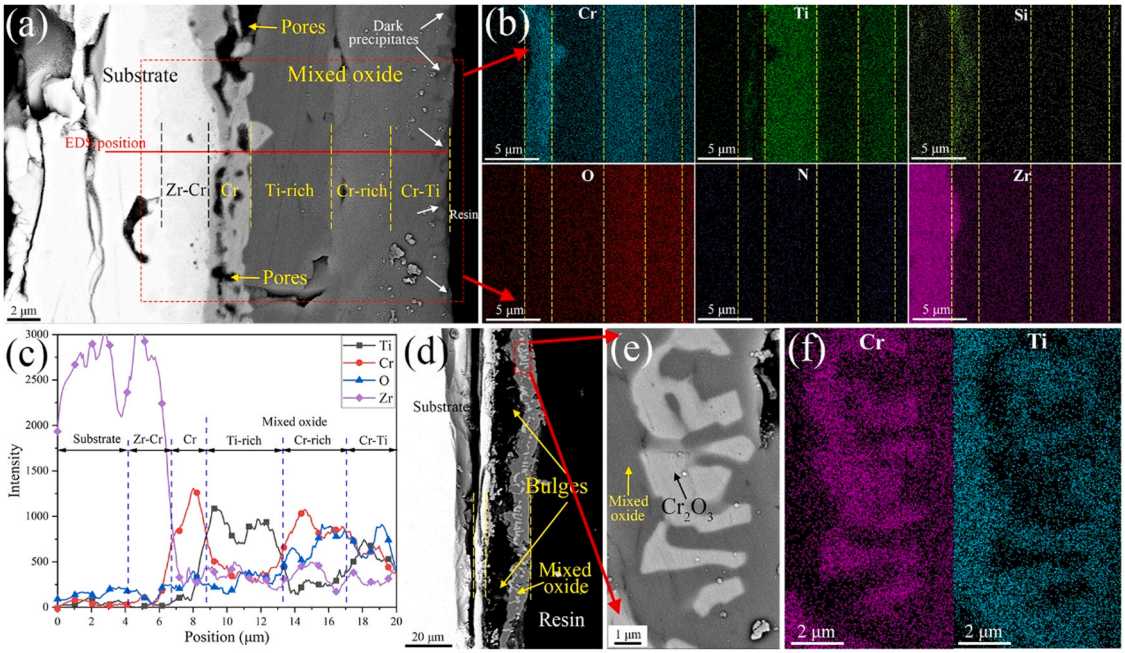

Fig. 11. Cross-sectional SEM characterization of the Cr-CrN/TiSiN-Cr-coated Zry-4 rod after oxidation in steam at 1200 °C for 3600 s: (a) SEM image of the coating, (b) EDS maps of the local region in (a), (c) EDS line scans of (c), (d) SEM image of the bulge region, (e) local microstructures in (d) at a higher magnification, and (f) EDS maps of (e).

by the outward diffusion of Ti and the inward diffusion of O through the oxide. A multilayer mixed oxide scale formed after oxidation. When the coating was oxidized at 1200 °C, the initial oxidation products of the multilayer coating were $(Cr_{1-x}Ti_x)_2O_3$ and Cr_2TiO_5 phases. Subsequently, with further outward diffusion of Ti, these two phases transformed into $(Cr_{1-y}Ti_y)_2O_3$ and $(Cr_{1-z}Ti_z)_2TiO_5$ phases owing to the replacement of the Cr atoms in the crystal lattice with Ti atoms. The content of the Cr_2TiO_5 phase decreased with an increase in the oxidation time. No TiO_2 phase was generated during oxidation.

(3) In the early stage of oxidation, the outward diffusion of Ti and Si led to the decomposition of the TiSiN layer, which further produced pores inside this layer. In the later stage of oxidation, the outward diffusion of Ti and Si left CrN in the innermost region of the coating. The remaining CrN decomposed into Cr, increasing the thickness of the Cr interlayer.

(4) Pores formed at the oxide/nitride coating interface after oxidation at 1200 °C for 1500 s. However, most of the pores were healed by the oxidation of the remaining nitride coating when the

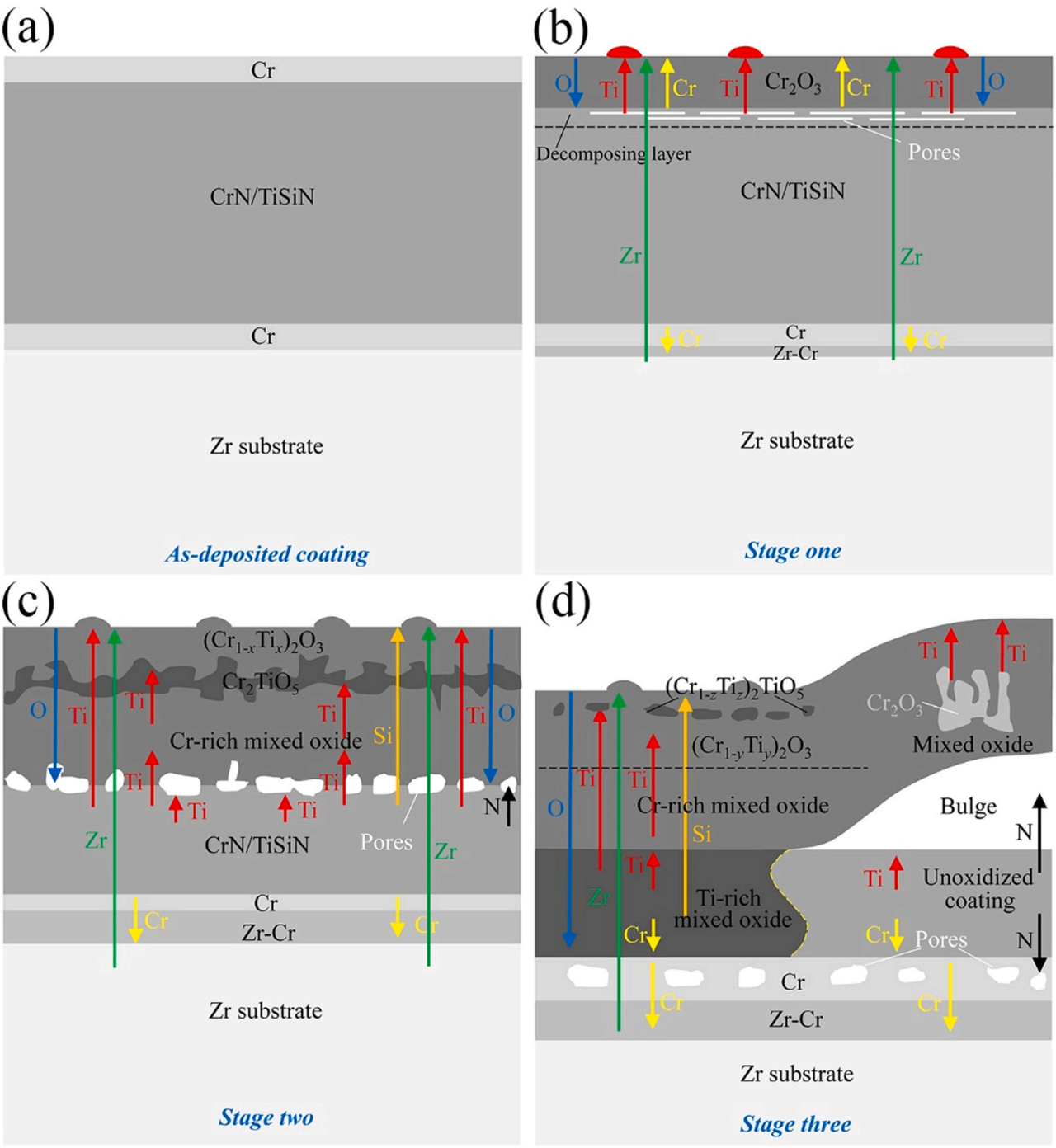

Fig. 12. Schematics describing the oxidation behavior and oxidation mechanism of the Cr-CrN/TiSiN-Cr-coated Zircaloy.

Table 2
The standard Gibbs free energy of the formation of different oxides at 1000 °C and 1200 °C.

$\triangle G_f$ (kJ/mol)	Cr_2O_3	TiO_2	SiO_2	ZrO_2
1000 °C	–538	–714	–683	–858
1200 °C	–505	–679	–649	–821

sample was oxidized for a longer time. Nevertheless, some of the pores grew by absorbing N_2 and eventually formed bulges.

(5) Zr in the Zircaloy substrate diffused outward to the coating. Finally, Zr reached the surface of the coating and formed ZrO_2 particles on the coating surface.

(6) Si in the superlattice coating diffused outward to the surface of the coating during oxidation and formed a SiO_2 protective layer.

CRediT authorship contribution statement

Junkai Liu : Conceptualization, Methodology, Investigation, Writing – original draft. **Zhe Hao** : Writing – review & editing, Investigation. **Zhexin Cui:** Investigation, Data curation. **Dayan Ma:**

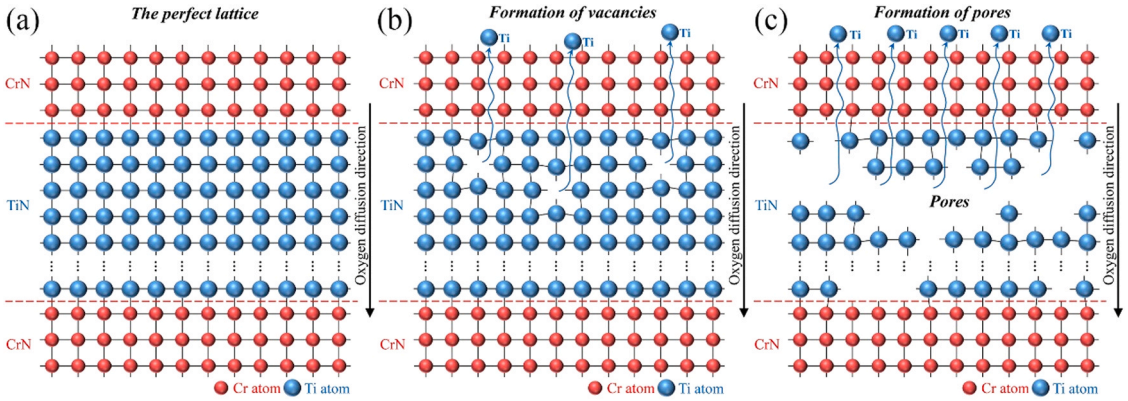

Fig. 13. Schematics describing the decomposition mechanisms of the CrN/TiSiN layer with a superlattice structure.

Conceptualization, Resources, Writing – review & editing. **Junqiang Lu:** Project administration, Resources. **Yanguang Cui** : Visualization. **Chong Li** : Conceptualization. **Wenbo Liu** : Writing – review & editing, Methodology. **Shijing Xie:** Writing – review & editing. **Ping Huang** : Resources. **Guanghai Bai** : Investigation, Conceptualization. **Di Yun:** Writing – review & editing, Supervision, Project administration.

Declaration of Competing Interest

The authors declare that they have no known competing financial interests or personal relationships that could have appeared to influence the work reported in this paper.

Data availability

The raw data required to reproduce these findings cannot be shared at this time as the data also forms part of an ongoing study. The processed data required to reproduce these findings cannot be shared at this time as the data also forms part of an ongoing study.

Acknowledgements

Financial support provided by the National Science and Technology Major Project, China (No. 2017ZX06002004), China Scholarship Council, China (No. 201906280379). We thank Mr. Zijun Ren, Ms. Jiao Li, and Mr. Chang Huang at Instrument Analysis Center of Xi'an Jiaotong University for their assistance with SEM, TEM, and XRD analysis, respectively.

References

[1] C. Lemaignan, Comprehensive nuclear materials!zirconium alloys: properties and characteristics, Compr. Nucl. Mater. (2012) 217–232.
[2] M. Guerain, C. Duriez, J. Grosseau-Poussard, M. Mermoux, Review of stress fields in zirconium alloys corrosion scales, Corros. Sci. 95 (2015) 11–21.
[3] S. Gou, B. Zhou, C. Chen, M. Yao, J. Peng, X. Liang, J. Zhang, Q. Li, Investigation of oxide layers formed on zircaloy-4 coarse-grained specimens corroded at 360° C in lithiated aqueous solution, Corros. Sci. 92 (2015) 237–244.
[4] T. Kim, J. Kim, K.J. Choi, S.C. Yoo, S. Kim, J.H. Kim, Phase transformation of oxide film in zirconium alloy in high temperature hydrogenated water, Corros. Sci. 99 (2015) 134–144.
[5] H. Kim, I. Kim, B. Choi, J. Park, A study of the breakaway oxidation behavior of zirconium cladding materials, J. Nucl. Mater. 418 (2011) 186–197.
[6] M.S. Slobodyan, S.K. Pavlov, G.E. Remnev, Corrosion and high-temperature steam oxidation of E110 alloy and its laser welds after ion irradiation, Corros. Sci. 152 (2019) 60–74.
[7] B. Mazères, C. Desgranges, C. Toffolon-Masclet, D. Monceau, Experimental study and numerical simulation of high temperature (1100–1250° C) oxidation of prior-oxidized zirconium alloy, Corros. Sci. 103 (2016) 10–19.
[8] C.M. Lee, D. Sohn, Enhanced high-temperature oxidation resistance of a zirconium alloy cladding by high-temperature preformed oxide on the cladding, Corros. Sci. 131 (2018) 116–125.
[9] K.A. Terrani, Accident tolerant fuel cladding development: promise, status, and challenges, J. Nucl. Mater. 501 (2018) 13–30.
[10] L.J. Ott, K.R. Robb, D. Wang, Preliminary assessment of accident-tolerant fuels on LWR performance during normal operation and under DB and BDB accident conditions, J. Nucl. Mater. 448 (2014) 520–533.
[11] B.A. Pint, K.A. Terrani, Y. Yamamoto, L.L. Snead, Material selection for accident tolerant fuel cladding, Metall. Mater. Trans. E 2 (2015) 190–196.
[12] C. Tang, M. Stueber, H.J. Seifert, M. Steinbrueck, Protective coatings on zirconium-based alloys as accident-tolerant fuel (ATF) claddings, Corros. Rev. 35 (2017) 141–165.
[13] D. Jin, N. Ni, Y. Guo, Z. Zou, X. Wang, F. Guo, X. Zhao, P. Xiao, Corrosion of the bonding at FeCrAl/Zr alloy interfaces in steam, J. Nucl. Mater. 508 (2018) 411–422.
[14] X. Han, J. Xue, S. Peng, H. Zhang, An interesting oxidation phenomenon of Cr coatings on Zry-4 substrates in high temperature steam environment, Corros. Sci. 156 (2019) 117–124.
[15] J. Brachet, E. Rouesne, J. Ribis, T. Guilbert, S. Urvoy, G. Nony, C. Toffolon-Masclet, M. Le Saux, N. Chaabane, H. Palancher, A. David, J. Bischoff, J. Augereau, E. Pouillier, High temperature steam oxidation of chromium-coated zirconium-based alloys: kinetics and process, Corros. Sci. 167 (2020), 108537.
[16] J. Liu, Z. Hao, Z. Cui, D. Ma, J. Lu, Y. Cui, C. Li, W. Liu, S. Xie, P. Hu, P. Huang, G. Bai, D. Yun, Oxidation behavior, thermal stability, and the coating/substrate interface evolution of CrN-coated Zircaloy under high-temperature steam, Corros. Sci. 185 (2021), 109416.
[17] J. Liu, Z. Cui, D. Ma, J. Lu, Y. Cui, C. Li, W. Liu, Z. Hao, P. Hu, M. Yao, P. Huang, G. Bai, D. Yun, Investigation of oxidation behaviors of coated Zircaloy as accident-tolerant fuel with CrAlN and CrAlSiN coatings in high-temperature steam, Corros. Sci. 175 (2020), 108896.
[18] T. Wei, R. Zhang, H. Yang, H. Liu, S. Qiu, Y. Wang, P. Du, K. He, X. Hu, C. Dong, Microstructure, corrosion resistance and oxidation behavior of Cr-coatings on Zircaloy-4 prepared by vacuum arc plasma deposition, Corros. Sci. 158 (2019), 108077.
[19] X. Han, C. Chen, Y. Tan, W. Feng, S. Peng, H. Zhang, A systematic study of the oxidation behavior of Cr coatings on Zry4 substrates in high temperature steam environment, Corros. Sci. 174 (2020), 108826.
[20] H. Yeom, B. Maier, G. Johnson, T. Dabney, M. Lenling, K. Sridharan, High temperature oxidation and microstructural evolution of cold spray chromium coatings on Zircaloy-4 in steam environments, J. Nucl. Mater. 526 (2019), 151737.
[21] E.B. Kashkarov, D.V. Sidelev, M.S. Syrtanov, C. Tang, M. Steinbrück, Oxidation kinetics of Cr-coated zirconium alloy: Effect of coating thickness and microstructure, Corros. Sci. 175 (2020), 108883.
[22] J. Yang, U. Stegmaier, C. Tang, M. Steinbrück, M. Große, S. Wang, H.J. Seifert, High temperature Cr-Zr interaction of two types of Cr-coated Zr alloys in inert gas environment, J. Nucl. Mater. 547 (2021), 152806.
[23] C. Meng, L. Yang, Y. Wu, J. Tan, W. Dang, X. He, X. Ma, Study of the oxidation behavior of CrN coating on Zr alloy in air, J. Nucl. Mater. 515 (2019) 354–369.
[24] S. Mato, G. Alcalá, M. Brizuela, R.E. Galindo, F.J. Pérez, J.C. Sánchez-López, Long-term high temperature oxidation of CrAl (Y) N coatings in steam atmosphere, Corros. Sci. 80 (2014) 453–460.
[25] N. Fukumoto, H. Ezura, T. Suzuki, Synthesis and oxidation resistance of TiAlSiN and multilayer TiAlSiN/CrAlN coating, Surf. Coat. Technol. 204 (2009) 902–906.
[26] P.H. Mayrhofer, F. Rovere, M. Moser, C. Strondl, R. Tietema, Thermally induced transitions of CrN thin films, Scr. Mater. 57 (2007) 249–252.
[27] A. Illana, E. Almandoz, G.G. Fuentes, F.J. Pérez, S. Mato, Comparative study of CrAlSiN monolayer and CrN/AlSiN superlattice multilayer coatings: behavior at high temperature in steam atmosphere, J. Alloy. Compd. 778 (2019) 652–661.
[28] S. Zhang, L. Wang, Q. Wang, M. Li, A superhard CrAlSiN superlattice coating deposited by multi-arc ion plating: I. Microstructure and mechanical properties, Surf. Coat. Technol. 214 (2013) 160–167.
[29] S. Zhang, L. Wang, Q. Wang, M. Li, A superhard CrAlSiN superlattice coating deposited by a multi-arc ion plating: II. Thermal stability and oxidation resistance, Surf. Coat. Technol. 214 (2013) 153–159.
[30] Y.X. Ou, J. Lin, S. Tong, H.L. Che, W.D. Sproul, M.K. Lei, Wear and corrosion resistance of CrN/TiN superlattice coatings deposited by a combined deep

oscillation magnetron sputtering and pulsed dc magnetron sputtering, Appl. Surf. Sci. 351 (2015) 332–343.
[31] L. Wang, M. Wang, H. Chen, Corrosion mechanism investigation of TiAlN/CrN superlattice coating by multi-arc ion plating in 3.5 wt% NaCl solution, Surf. Coat. Technol. 391 (2020), 125660.
[32] C. Fan, Q. Li, J. Ding, Y. Liang, Z. Shang, J. Li, R. Su, J. Cho, D. Chen, Y. Wang, J. Wang, H. Wang, X. Zhang, Helium irradiation induced ultra-high strength nanotwinned Cu with nanovoids, Acta Mater. 177 (2019) 107–120.
[33] D. Zhang, X. Zuo, Z. Wang, H. Li, R. Chen, A. Wang, P. Ke, Comparative study on protective properties of CrN coatings on the ABS substrate by DCMS and HiPIMS techniques, Surf. Coat. Technol. 394 (2020), 125890.
[34] X. Cai, Y. Gao, F. Cai, L. Zhang, S. Zhang, Effects of multi-layer structure on microstructure, wear and erosion performance of the Cr/CrN films on Ti alloy substrate, Appl. Surf. Sci. 483 (2019) 661–669.
[35] H. Chen, Y. Chan, J. Lee, J. Duh, Oxidation behavior of Si-doped nanocomposite CrAlSiN coatings. Surface and coatings technology 205 (2010) 1189–1194.
[36] C. Puneet, K. Valleti, A. Venu Gopal, S.V. Joshi, CrAlSiN nanocomposite thin films for high-speed machining applications, Mater. Manuf. Process. 33 (2018) 371–377.
[37] A.M. Huntz, Stresses in NiO, Cr2O3 and Al2O3 oxide scales, Mater. Sci. Eng. A 201 (1995) 211–228.
[38] Z. Liu, J. Yang, Y. Qian, J. Xu, J. Zuo, M. Li, High temperature oxidation behavior of quaternary ordered (Cr2/3Ti1/3)3AlC2-based MAX ceramic, Corros. Sci. 183 (2021), 109317.
[39] L. Chen, J. Paulitsch, Y. Du, P.H. Mayrhofer, Thermal stability and oxidation resistance of Ti–Al–N coatings, Surf. Coat. Technol. 206 (2012) 2954–2960.
[40] C. Tang, M. Steinbrueck, M. Stueber, M. Grosse, X. Yu, S. Ulrich, H.J. Seifert, Deposition, characterization and high-temperature steam oxidation behavior of single-phase Ti2AlC-coated Zircaloy-4, Corros. Sci. 135 (2018) 87–98.
[41] X. Li, L. Zheng, Y. Qian, J. Xu, M. Li, Breakaway oxidation of Ti3AlC2 during long-term exposure in air at 1100 °C, Corros. Sci. 104 (2016) 112–122.
[42] X. Li, L. Zheng, Y. Qian, J. Xu, M. Li, Thickness-dependent oxidation behaviors of Ti3AlC2 foils at 1100 °C in air, Corros. Sci. 185 (2021), 109431.
[43] G.S. Kim, S.Y. Lee, J.H. Hahn, S.Y. Lee, Synthesis of CrN/AlN superlattice coatings using closed-field unbalanced magnetron sputtering process, Surf. Coat. Technol. 171 (2003) 91–95.
[44] L. Wang, M. Wang, H. Chen, Corrosion mechanism investigation of TiAlN/CrN superlattice coating by multi-arc ion plating in 3.5 wt% NaCl solution, Surf. Coat. Technol. 391 (2020), 125660.
[45] J. Park, Y. Baik, The crystalline structure, hardness and thermal stability of AlN/CrN superlattice coating prepared by D.C. magnetron sputtering, Surf. Coat. Technol. 200 (2005) 1519–1523.
[46] M. Schlogl, J. Paulitsch, P.H. Mayrhofer, Thermal stability of CrN/AlN superlattice coatings, Surf. Coat. Technol. 240 (2014) 250–254.
[47] S.C. Tsai, A.M. Huntz, C. Dolin, Growth mechanism of Cr2O3 scales: oxygen and chromium diffusion, oxidation kinetics and effect of yttrium, Mater. Sci. Eng. A 212 (1996) 6–13.
[48] S.C. Tsa, A.M. Huntz, J. Philibert, Diffusion of 54Cr and 18O in Cr2O 3 scales and growth mechanism, Defect Diffus. Forum 143 (1997) 1195–1200.
[49] D.B. Lee, M.H. Kim, Y.C. Lee, S.C. Kwon, High temperature oxidation of TiCrN coatings deposited on a steel substrate by ion plating, Surf. Coat. Technol. 141 (2001) 232–239.
[50] B.A. Pint, Experimental observations in support of the dynamic-segregation theory to explain the reactive-element effect, Oxid. Met. 45 (1996) 1–37.
[51] M. Wittmer, J. Noser, H. Melchior, Oxidation kinetics of TiN thin films, J. Appl. Phys. 52 (1981) 6659–6664.
[52] K.H. Lee, S.J. Jung, J.J. Lee, C. Park, High-temperature oxidation behaviors of the (Ti 1− x Cr x) N coatings, J. Mater. Sci. Lett. 21 (2002) 423–425.
[53] D.B. Lee, TEM study on oxidized TiCrN coatings ion-plated on a steel substrate, Surf. Coat. Technol. 173 (2003) 81–86.
[54] S. Kamiya, S. Hirano, S. Somiya, The compound Cr2TiO5 in the system Cr2O3·TiO2, J. Solid State Chem. 28 (1979) 21–28.